



Boosting oxygen electrocatalytic performance of Cu atom by engineering the *d*-band center via secondary heteroatomic phosphorus modulation

Lei Wang^{a,b}, Wen-Wen Tian^b, Wenlin Zhang^{a,*}, Fengshou Yu^{a,*}, Zhong-Yong Yuan^{b,*}

^a National-Local Joint Engineering Laboratory for Energy Conservation in Chemical Process Integration and Resources Utilization, School of Chemical Engineering and Technology, Hebei University of Technology, Tianjin 300130, China

^b National Institute for Advanced Materials, School of Materials Science and Engineering, Smart Sensing Interdisciplinary Science Center, Nankai University, Tianjin 300350, China

ARTICLE INFO

Keywords:

Secondary heteroatomic phosphorus
Copper single atom
Zinc-air batteries
Oxygen reduction reaction
d-band center

ABSTRACT

Atomically dispersed catalysts have been widely explored for some reactions, but it remains a challenge to modulate the electronic structure of the center metal for enhancing the electrochemical activity. Herein, the electrochemical activity of copper single-atom catalyst (Cu SAC) was significantly improved by doping secondary heteroatomic phosphorus to engineer the *d*-band center of Cu atoms, which was named Cu SAC/P. In alkaline media, the Cu SAC/P-700 catalyst exhibited excellent oxygen reduction reaction (ORR) performance with a higher half-wave potential than Cu SAC-700, even better than the state-of-the-art 20 wt% Pt/C 20 mV. The oxygen electroactivity coefficient was only 0.76 V, achieving good performance in zinc-air battery tests. Density functional theory calculations suggested that phosphorus effectively modulated the density of states and the *d*-band center of Cu atoms. It improved the adsorption of the reaction intermediates and facilitated to trap them on Cu atoms, thus boosting the ORR activity of the catalyst.

1. Introduction

With the advantages of high theoretical energy density, inherent safety, and low manufacturing cost, zinc-air batteries (ZABs) are considered to be the next-generation cutting-edge technology for sustainable energy storage [1–4]. However, the main challenge facing this technology is the slow kinetics caused by the four-electron-transfer pathway in oxygen reduction reaction (ORR) and oxygen evolution reaction (OER), which limits the discharge and charge performance of ZABs, respectively [5–8]. Pt-based catalysts are acknowledged as the superior electrocatalysts for ORR, but the scarcity, high cost and poor durability of the noble metal Pt greatly limit the wide application of Pt-based catalysts in ZABs [9–12]. Therefore, it is of great application value to develop efficient and stable non-noble metal ORR catalysts to replace Pt-based catalysts.

In recent years, single-atom catalysts (SACs) composed of transition metals (M-N-C, M refers to Fe, Co, Ni, Cu, etc.) embedded in the carbon material have shown high atomic efficiency and promising ORR activity, which are considered an ideal alternative to the Pt-based catalyst [13–15]. Cu SACs have been widely reported for ORR, nevertheless, most of these catalysts contain only Cu-N_x moiety [16–19], and their

electronic structures are not controllably optimized, resulting in too strong or too weak adsorption of ORR intermediates at active sites and limiting the optimal ORR activity [20,21]. The doping of secondary heteroatoms (B, O, P, S, etc.) into metal-nitrogen material catalysts can tune the coordination environment of the M-N_x moiety and the density of states distribution for active sites, which improves the electrochemical activity of the catalyst [22,23]. It has been reported that doping the secondary heteroatom (e.g. P) into catalysts leads to highly localized states near the Fermi level [24]. In addition, due to the lower electronegativity and good electron-donating properties of P [25], P-doping changes the charge density of Cu-N_x moiety and effectively optimizes the density of states of the copper atom, thus enhancing the binding strength of Cu atoms to reaction intermediates and boosting the ORR activity [26–28].

In this study, a highly efficient ORR catalyst was developed by introducing secondary heteroatomic phosphorus into a copper single-atom catalyst (Cu SAC), with self-assembled polypyrrole hydrogel as the precursor and phytic acid as the P source. The experimental results showed that the Cu SAC/P-700 catalyst exhibited a superior ORR activity compared with the Cu SAC-700 catalyst containing only Cu-N_x moiety, where the half-wave potential of Cu SAC/P-700 ($E_{1/2}$ = 0.87 V)

* Corresponding authors.

E-mail addresses: ctstzwl@163.com (W. Zhang), yfsh@hebut.edu.cn (F. Yu), zyyuan@nankai.edu.cn (Z.-Y. Yuan).

<https://doi.org/10.1016/j.apcatb.2023.123043>

Received 14 April 2023; Received in revised form 22 June 2023; Accepted 23 June 2023

Available online 29 June 2023

0926-3373/© 2023 Elsevier B.V. All rights reserved.

was 40 mV higher than that of Cu SAC-700 ($E_{1/2} = 0.83$ V) with 20 mV higher than commercial Pt/C catalyst ($E_{1/2} = 0.85$ V) in alkaline media. The catalyst also exhibited promising ORR activity in acidic media. Density functional theory (DFT) calculations demonstrated that phosphorus effectively modulated the density of states of the Cu atom and engineered its d -band center toward the Fermi energy level, compared to the Cu SAC catalyst, thus modulating the adsorption behavior of the catalyst on the ORR intermediate. Additionally, in this work, the constructed zinc-air battery with Cu SAC/P-700 catalyst as the air cathode exhibited good discharge performance and cycling stability, which was obviously superior to the commercial Pt/C catalyst.

2. Experimental section

2.1. Materials and chemicals

All chemicals and solvents were used as received without further purification. Copper(II) chloride dihydrate ($\text{CuCl}_2 \cdot 2\text{H}_2\text{O}$ 98%), ethanol ($\text{C}_2\text{H}_5\text{OH}$ 99.8%), ammonium persulphate ($(\text{NH}_4)_2\text{S}_2\text{O}_8$ 99.99% metals basis), phytic acid ($\text{C}_6\text{H}_{18}\text{O}_{24}\text{P}_6$ 50%, wt./wt. in water), potassium hydroxide (KOH, AR) and pyrrole ($\text{C}_4\text{H}_5\text{N}$ 99%) were purchased from Aladdin Industrial Inc. Deionized water (H_2O) and hydrochloric acid (37 wt%) were purchased from Kermel. Commercial Pt/C (20 wt%) and Nafion (5 wt%) were purchased from Suzhou Yilongsheng Energy

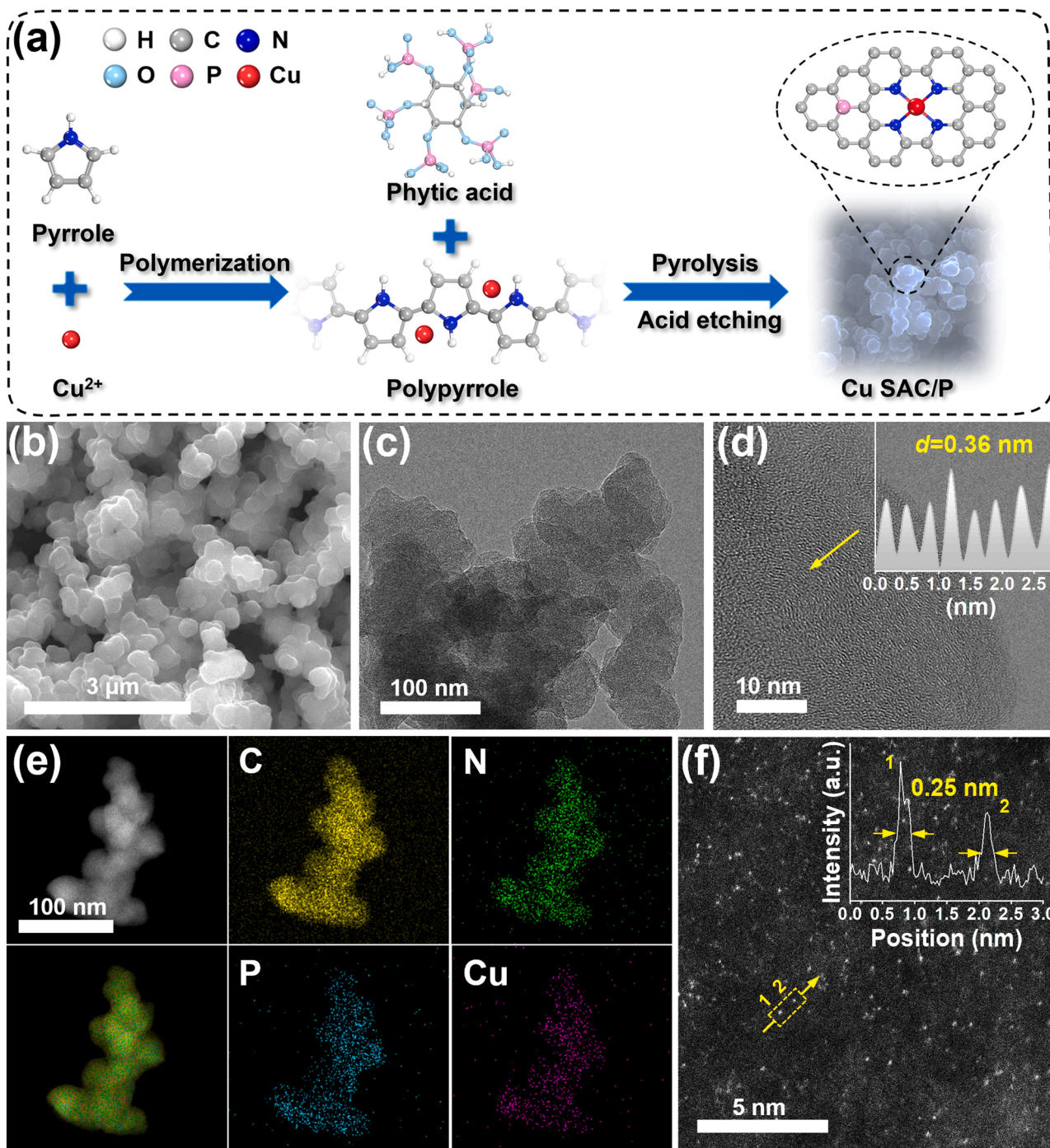


Fig. 1. (a) Synthesis process and structure of Cu SAC/P catalysts. (b) SEM, (c) TEM, (d) HRTEM. (e) HAADF-STEM image and corresponding EDS spectroscopy elemental mapping images of C, N, Cu, P, and overlap. (f) AC HAADF-STEM image of Cu SAC/P-700.

Technology Co., Ltd.

2.2. Synthesis of polypyrrole (PPy) hydrogel

415 μL (6 mmol) pyrrole monomer was mixed with 2 mL of ethanol/deionized water ($V/V=1:1$) mixture. 2.5572 g (15 mmol) of $\text{CuCl}_2 \cdot 2\text{H}_2\text{O}$ was added to the 4 mL of ethanol/deionized water ($V/V=1:1$) mixture and ultrasonically dispersed. The above two reagents were cooled to 4 °C, which were quickly mixed, and then aged for 24 h. The polypyrrole (PPy) hydrogel was immersed in a mixture of ethanol/deionized water ($V/V=1:1$) and kept for 24 h to remove by-products. Finally, the PPy hydrogel was freeze-dried.

2.3. Preparation of Cu SAC/P catalysts

1.00 g of dried PPy hydrogel was ultrasonically dispersed with 0.921 mL (1 mmol) of phytic acid and then pyrolyzed at 600, 700, and 800 °C for 2 h under an argon atmosphere with a heating rate of 5 °C/min [24]. The pyrolysis products were placed in a 6 M hydrochloric acid solution and stirred at 80 °C for 24 h, filtered and washed with plenty of deionized water, and finally dried under vacuum at room temperature. The products of pyrolysis at different temperatures were labeled as Cu SAC/P-600, Cu SAC/P-700, and Cu SAC/P-800, respectively.

2.4. Preparation of Cu SAC-700 catalyst

The Cu SAC-700 catalyst was prepared in the same way as the Cu SAC/P-700 catalyst, except that phytic acid was not added.

3. Results and discussion

3.1. Secondary heteroatomic modification

Cu SAC/P catalysts were fabricated by doping secondary heteroatomic P into self-assembled polypyrrole hydrogels, and the preparation schematic is shown in Fig. 1a. To investigate the optimal temperature for preparing Cu SAC/P catalysts, the samples were fabricated under three different pyrolysis temperatures (600, 700, and 800 °C), which were noted as Cu SAC/P-600, Cu SAC/P-700, and Cu SAC/P-800, respectively. Meanwhile, to explore the doping effect of P, Cu SAC catalyst was also prepared using the same method at the optimal reaction temperature. With the aid of scanning electron microscopy (SEM, Fig. 1b and S1), Cu SAC and Cu SAC/P catalysts had similar morphological characteristics, where the surface of the catalyst was covered with small particles with diameters of about 200 nm.

In transmission electron microscopy (TEM, Fig. 1c and S2) images, no obvious metal nanoparticles were detected in various catalysts. Meanwhile, in the X-ray diffractograms (XRD, Fig. S3) of the Cu SAC/P catalysts and the Cu SAC-700 catalyst, only the (002) and (101) planes of graphitic carbon were observed without the diffraction peaks of metal monomers. The high-resolution transmission electron microscopy (HRTEM) image showed that the Cu SAC/P-700 catalyst had a graphite lattice with an average spacing of 0.36 nm in Fig. 1d. High-angle annular dark-field scanning transmission electron microscopy (HAADF-STEM) image and corresponding elemental mapping images (Fig. 1e) further confirmed that the C, N, Cu, and P elements were uniformly distributed throughout Cu SAC/P-700. In the Aberration-corrected HAADF-STEM image (AC HAADF-STEM, Fig. 1f), uniformly distributed bright dots in the Cu SAC/P-700 can be clearly observed. The linear scan analysis along the arrow direction showed that the half-peak width of individual bright spots was about 0.25 nm, which was consistent with the diameter of copper atoms [29,30]. From Raman spectra (Fig. S4), the higher I_D/I_G ratio can be seen in Cu SAC/P-700 compared to that of Cu SAC-700. Interestingly, the I_D/I_G ratio of Cu SAC/P catalysts calcined at 700 °C was slightly larger than those calcined at 600 and 800 °C. Meanwhile, it was also confirmed that doping with

heteroatomic phosphorus was beneficial for oxygen adsorption, through temperature-programmed desorption of O_2 (TPD, Fig. S5) [31,32].

X-ray photoelectron spectroscopy (XPS, Fig. 2a) was used to reveal the chemical composition and elemental states in Cu SAC and Cu SAC/P catalysts. There were C 1s, O 1s, N 1s, and Cu 2p elemental signals in the total XPS spectrum of Cu SAC-700, with an additional P 2p elemental peak in the Cu SAC/P catalyst. Also, the high-resolution spectra measured for C 1s of the Cu SAC/P catalysts (Fig. S7) showed an additional peak (286.5 eV) attributable to the C-P bond [33,34], indicating that the heteroatomic P had been successfully doped into the Cu SAC/P catalyst. The N 1s spectra (Fig. 2b and S8) showed five deconvoluted components, corresponding to pyridinic N (398.3 ± 0.1 eV), Cu-N (399.0 ± 0.1 eV), pyrrolic N (400.4 ± 0.1 eV), graphitic N (401.1 ± 0.1 eV) and oxidized N (403.9 ± 0.1 eV) [35–37], respectively. Particularly, the relative ratios of the deconvoluted N species indicated that the Cu SAC/P-700 catalyst (Fig. 2c) had the highest pyridinic N and Cu-N bond content. Meanwhile, XPS and inductively coupled plasma optical emission spectrometry (ICP-OES) studies (Table S1) and thermogravimetry curves (Fig. S8) showed that Cu SAC/P-700 also had a similar copper content with Cu SAC-700. The high-resolution P 2p spectra (Fig. S9) of Cu SAC/P catalysts displayed two peaks, corresponding to the P-C bond (132.6 eV) and P-O bond (133.8 eV) [38], respectively. The peaks observed at 932.6 and 952.3 eV in the Cu 2p region of Cu SAC/P-700 were attributed to the Cu $2p_{3/2}$ and Cu $2p_{1/2}$ orbitals of Cu^+ , respectively. The observation of binding energies locating at 934.9 and 954.7 eV (Fig. S10) were indicative of Cu^{2+} (Fig. S10a) [39,40]. Furthermore, the Cu LMM Auger spectrum (Fig. S10b) further indicated the existence of both Cu^+ and Cu^{2+} in Cu SAC/P-700 [41,42].

To further investigate the states of the copper species dispersed in the Cu SAC/P-700 catalyst, X-ray absorption near-edge structure (XANES) and extended X-ray absorption fine structure (EXAFS) spectra were conducted with copper foil, cuprous (I) oxide (Cu_2O), cupric oxide (CuO) and copper (II) phthalocyanine (CuPc) as reference. The K-edge absorption spectrum of Cu SAC/P-700 (Fig. 2d) was lower than that of CuO and CuPc , but higher than that of Cu_2O , indicating that the valence state of Cu was between Cu^{I} and Cu^{II} [35,43]. The Fourier-transformed (FT) k^3 -weighted (FT-EXAFS) curves of the Cu SAC/P-700 sample (Fig. 2e) only showed the main peak position appearing at 1.5 Å, which can be attributed to the Cu-N first coordination shell [44], and there is no peak at 2.2 Å attributed to Cu-Cu bond [45]. The Cu K-edge wavelet transform (WT-EXAFS) of Cu SAC/P-700 showed a sole contour peak with a maximum strength of approximately 3.7 \AA^{-1} , which was closely approximated to that of CuPc with Cu- N_4 bonds, indicating the presence of Cu-N coordination in Cu SAC/P-700 [41]. Compared with the WT-EXAFS signal of Cu foil, no intensity maxima attributed to Cu-Cu contribution was detected. The above results proved that only isolated Cu atoms existed on Cu SAC/P-700, which agreed well with the AC HAADF-STEM observation. The fine coordination environment of the Cu site was further determined by EXAFS fitting results (Fig. 2g, h), and the curve was highly agreed with the Cu SAC/P structure (as presented in Fig. 2g) [46], which indicated that the Cu SAC/P-700 was a Cu- N_4 structure with P embedded into the carbon substrate. The EXAFS coordination information table of Cu SAC/P-700 (Table S2) showed that the coordination number of Cu-N was 4, which further supports our conclusion.

3.2. Catalytic roles of Cu atom and secondary heteroatomic P

The ORR performance was evaluated with cyclic voltammograms (CV) for different catalysts in alkaline media saturated with N_2 or O_2 . In O_2 -saturated 0.1 M KOH solution, Cu SAC/P-700 exhibited a distinct cathodic peak corresponding to the ORR (Fig. S11). From the linear sweep voltammetry (LSV, Fig. S12), P/N-C-700 presented superior onset potentials (E_0) and half-wave potentials ($E_{1/2}$) compared to that of N-C-700. Also, Cu SAC/P-700 exhibited more outstanding E_0 of 0.96 V (vs.

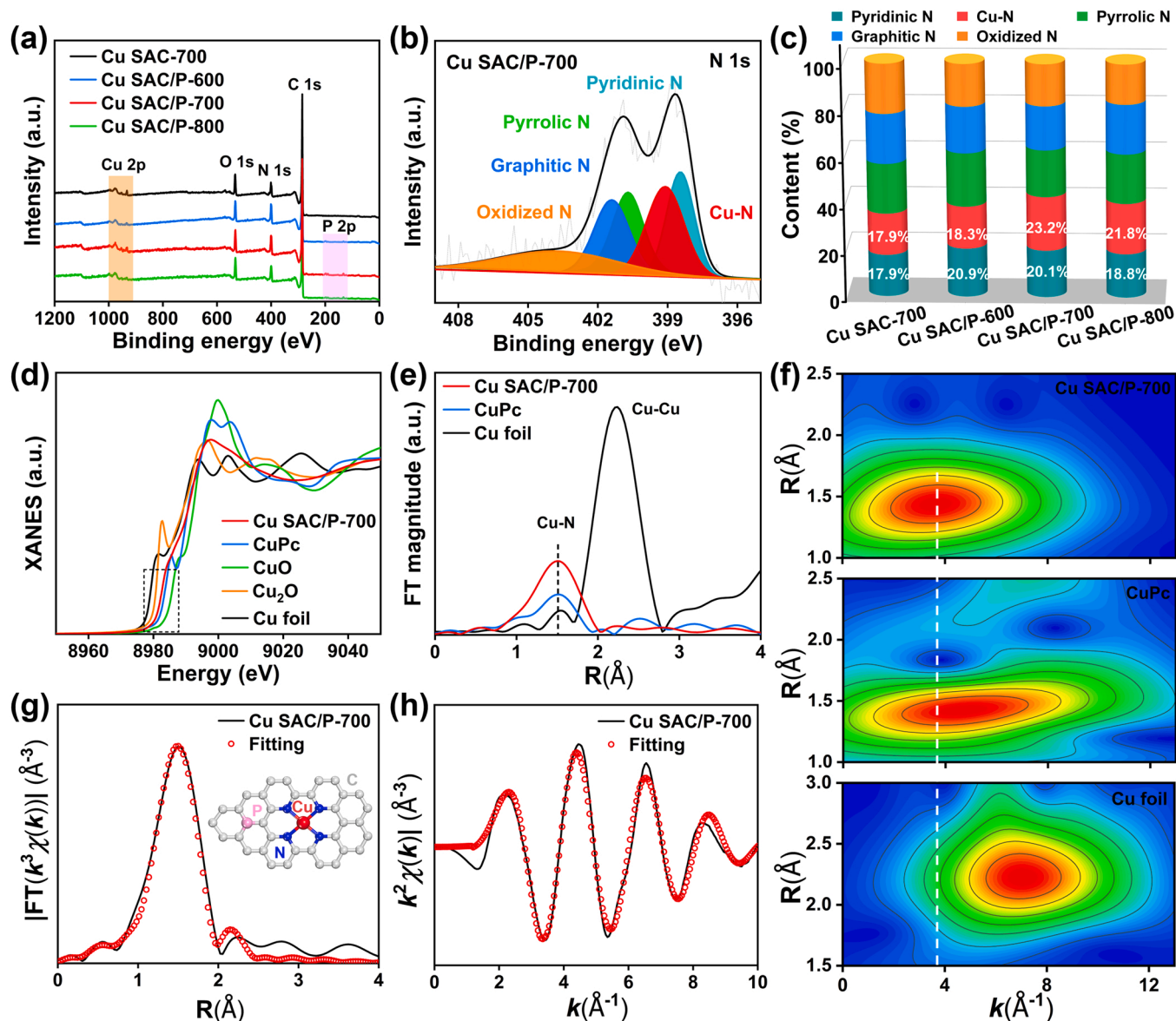


Fig. 2. (a) The survey XPS spectra of Cu SAC-700, Cu SAC/P-600, Cu SAC/P-700, and Cu SAC/P-800. (b) N 1s XPS spectra of Cu SAC/P-700. (c) Relative ratios of the deconvoluted N species for different samples were calculated from the high-resolution N 1s XPS spectra. (d) XANES spectra at Cu K-edge of Cu foil, Cu₂O, CuO, CuPc, and Cu SAC/P-700. (e) Fourier transformed EXAFS spectra of the Cu K-edge EXAFS for Cu SAC/P-700. (f) Wavelet transform-EXAFS of Cu foil, CuPc, and Cu SAC/P-700. (g, h) The corresponding EXAFS fitting curves of Cu SAC/P-700 at R and k space, respectively.

RHE) and $E_{1/2}$ of 0.87 V, compared to that of Cu SAC-700 ($E_0 = 0.92$ V, $E_{1/2} = 0.83$ V, Fig. S12), implying that the introduction of the secondary heteroatomic P may effectively boost the ORR activity of catalysts. At the same time, Cu SAC/P-700 presented the highest ORR activity among Cu SAC/P catalysts (Fig. 3a), which was more positive than that of the state-of-the-art Pt/C catalyst ($E_{1/2} = 0.85$ V, Fig. 3b) by about 20 mV, and surpassed many of the reported carbon-based catalysts (Table S3). Notably, the Cu SAC/P-700 catalyst performed the highest kinetic current density (j_k) of 10.3 mA cm⁻² at 0.85 V, about 2 times higher than that of Pt/C ($j_k = 5.1$ mA cm⁻²) [47,48], and significantly higher than that of other catalysts (Fig. 3a, S13 and S14). The activity of Cu atoms loaded into the samples was normalized and the turnover frequency (TOF) curves of different catalysts were calculated. It was found that Cu SAC/P-700 also had the highest ORR activity (Fig. S14) [48]. As demonstrated in Fig. 3c, Cu SAC/P-700 exhibited the lowest Tafel slope of 72.4 mV dec⁻¹, which was significantly lower than that of Pt/C and Cu SAC-700, implying that the Cu SAC/P-700 had faster kinetics for ORR [32]. To obtain more ORR kinetics information about the samples, the

voltammograms at different rotational speeds were executed by using a rotated disk electrode (RDE, Fig. S15). The current density of Cu SAC/P-700 increased upon increasing rotation speed from 400 to 2025 rpm, and the well-linearized Koutecky-Levich (K-L) plots in Fig. S15 indicated the oxygen-first-order reaction of oxygen [49]. To clarify the reaction pathway of ORR, the number of electron transfers (n) for each oxygen molecule in different samples was calculated by using the K-L equation. The n value of Cu SAC/P-700 was 3.94, significantly higher than that of Cu SAC-700 (3.85), implying a typical four-electron transfer pathway for phosphorus-doped catalyst (Fig. S16). The n and hydrogen peroxide yield (H₂O₂%) were calculated by using a rotating ring disk electrode (RRDE, Figs. S17 and 3d). From 0.20–0.80 V, the n for Cu SAC/P-700 was in the range of 3.90–3.99 and the H₂O₂% was less than 5% (Fig. 3d), which was comparable to Pt/C. Meanwhile, Cu SAC/P-700 also exhibited encouraging electrochemical performance with $E_{1/2}$ of 0.75 V in acidic medium, which was close to that of the Pt/C catalyst (0.83 V). After 5 000 redox cycles, compared to Pt/C, no significant change was observed in the $E_{1/2}$ of Cu SAC/P-700 (Fig. S18). As

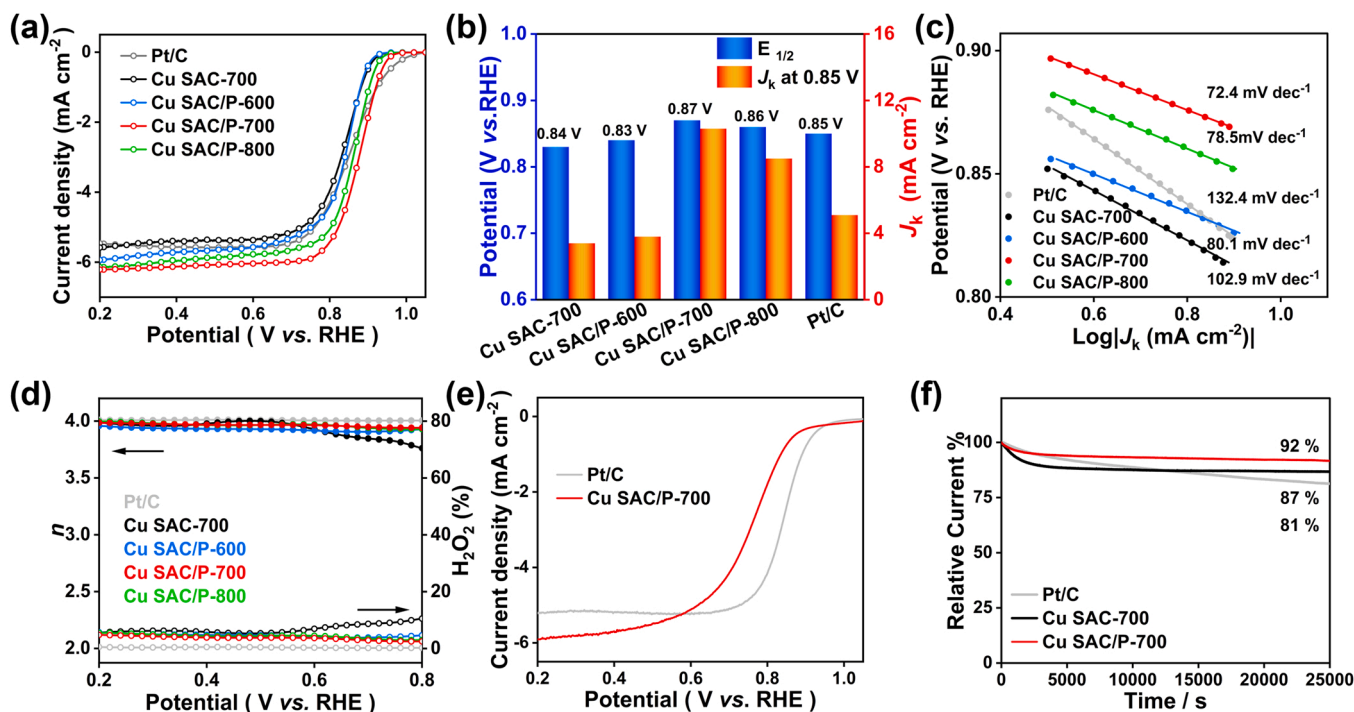


Fig. 3. (a) LSV curves of different catalysts in O₂-saturated 0.1 M KOH solution at 1600 rpm. (b) Half-wave potential and J_k at 0.85 V. (c) Tafel slope, and (d) Electron transfer number (top) and H₂O₂ yield (bottom) of various catalysts. (e) LSV curves of Pt/C and Cu SAC/P-700 in O₂-saturated 0.1 M HClO₄ solution. (f) Current-time chronoamperometric responses of Pt/C, Cu SAC-700, and Cu SAC/P-700 in O₂-saturated 0.1 M KOH solution.

evidenced in Fig. 3f, the ORR current retention rate of Cu SAC/P-700 catalyst remained 92% after 25, 000s by the chronoamperometric test at 0.70 V, which was better than that of Cu SAC-700 (87%) and Pt/C (81%), indicating the outstanding durability of Cu SAC/P-700. After adding 3 M methanol, there was also no significant current oscillation of Cu SAC/P-700 in Fig. S19, indicating that Cu SAC/P-700 exhibited

strong methanol tolerance.

Strikingly, Cu SAC/P-700 also exhibited oxygen evolution reaction (OER) electrochemical performance with 1.63 V at 10 mA cm⁻² (E_{10}) in 0.1 M KOH solution (Fig. S20). Due to the small oxygen electrode activity [50] (ΔE , Fig. S20) and exceptional bifunctional catalytic activity of Cu SAC/P-700, the Cu SAC/P-700 catalyst was further applied in

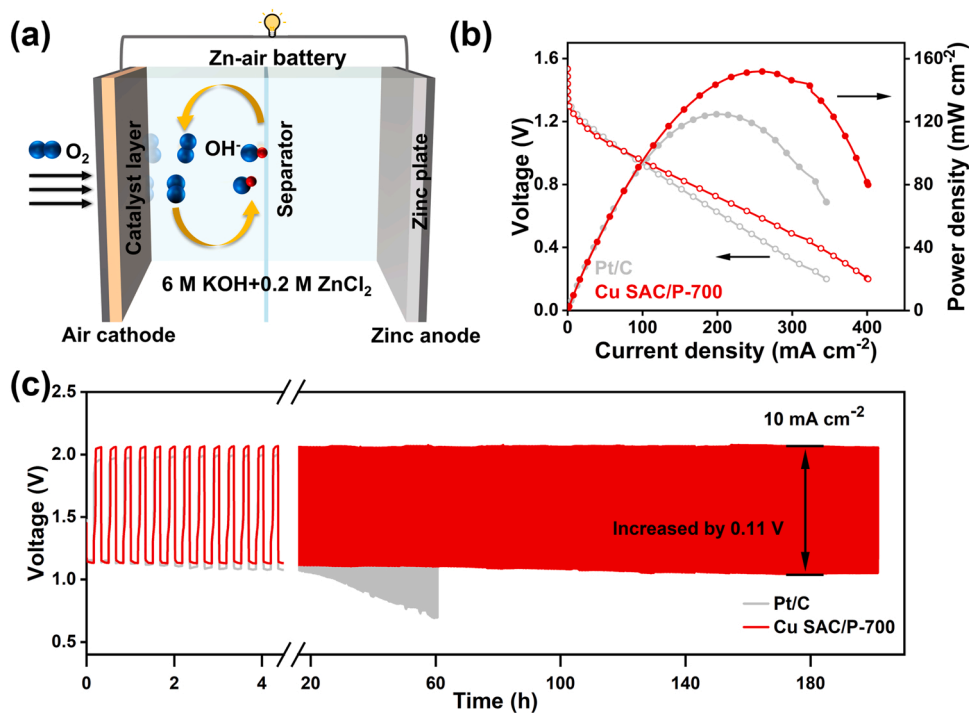


Fig. 4. (a) Schematic of a rechargeable Zinc-air battery. (b) Discharge polarization curves and power density plots of Pt/C and Cu SAC/P-700. (c) Entire charge and discharge cycling performance of rechargeable zinc-air batteries based on Pt/C and Cu SAC/P-700 catalysts at 10 mA cm⁻².

zinc-air batteries (ZABs) to explore practical performance in energy devices.

3.3. Application in device

As evidenced in Fig. 4a, the Cu SAC/P-700 catalyst served as cathode material for the ZAB, and the ZAB based on Pt/C was also constructed for comparison. Cu SAC/P-700-based ZAB exhibited a similar open-circuit voltage to that assembled with Pt/C (Fig. S21a). As shown in Fig. S21b, the specific capacity of Cu SAC/P-700-based ZAB is 766 mAh g_{Zn}^{-1} (coulombic efficiency: 93.4% of the theoretical capacity, 820 mAh g_{Zn}^{-1}) at a current density of 10 mA cm^{-2} , superior to that of Pt/C-based ZAB (725 mAh g_{Zn}^{-1}), which manifested that Cu SAC/P-700-based ZAB had more excellent coulombic efficiency. Besides, the peak power density of the Cu SAC/P-700-based ZAB was up to 152 mW cm^{-2} at a current density of 261 mA cm^{-2} , also higher than that of Pt/C-based ZAB (124 mW cm^{-2} , Fig. 4b). Two primary Cu SAC/P-700-based ZABs were connected in series, which could well power the LED display (Fig. S22). As demonstrated in Fig. 4c, in terms of entire charge and discharge cycling stability, the Cu SAC/P-700-based ZAB kept stable for 202 h at 10 mA cm^{-2} , with a slight increase of 0.11 V of voltage gap. By contrast, an obvious voltage attenuation during the test of charge/discharge cycling for 61 h was observed for Pt/C-based ZAB. These clearly demonstrated that the Cu SAC/P-700-based ZAB had good electrochemical activity and outperformed a large number of the reported zinc-air batteries (Table S4), displaying its application potential in the advanced energy storage field.

3.4. DFT calculations

To explore the intrinsic properties change and the mechanism of ORR activity enhancement, the DFT calculations were further performed. Meanwhile, the four possible models of Cu SAC-700 and Cu SAC/P-700 were built and geometry optimized, labeled as Cu SAC, Cu SAC/P-1, Cu SAC/P-2, and Cu SAC/P-3 (Fig. S23). As shown in Fig. 5a and Fig. S24, the Gibbs free energy of the reactant in each elementary step of the ORR pathway was calculated at 0 V and 1.23 V overpotential.

For Cu SAC, the first elementary electrochemical step (the OOH* intermediates formation step, 1.04 eV) was the rate-determining step (RDS, Fig. 5a). However, for Cu SAC/P-1, Cu SAC/P-2, and Cu SAC/P-3, the overcoming energy of OOH* intermediate formation step was only 0.29 eV, 0.75 eV, and 0.85 eV, which were significantly lower than that of Cu SAC. In addition, from the Sabatier principle, the optimal catalyst located at the vertex of the volcano curves plot generally had the best electrochemical performance [51,52]. The ORR activity and O* adsorption free energy of Cu SAC were far from the top of the volcano curves plot, indicating that the O* adsorption free energy of Cu SAC was so weak, resulting in a suboptimal ORR activity. In contrast, the O* adsorption free energy of the three P-doped catalyst models showed moderate binding strength and more significant enhancement of ORR activity [53], especially Cu SAC/P-1, which ORR overpotential was only 0.56 V (the formation of O* intermediate), even better than that of the noble metal single-atom catalyst [54] (Pt SAC 0.67 V, Fig. 5b). The charge density of the Cu-N₄ moiety would be changed due to the electron-donating properties of the secondary heteroatomic P, which might affect the adsorption of the intermediate [26] (Fig. S25). Meanwhile, the density of states (DOS) and projected density of states (PDOS) were investigated to explore the change in electronic interactions and adsorption strength of the intermediate. The results of DOS for Cu SAC and Cu SAC/P-1 illustrated that the Cu SAC/P-1 had higher density states at the Fermi level, compared to Cu SAC (Fig. S26), suggesting that Cu SAC/P-1 had higher electronic conductivity, which was more conducive to charge transfer in electrochemical processes [55,56]. From the PDOS of orbital interaction in Cu SAC and Cu SAC/P-1, there was a more obvious overlap between Cu 3d and P 3p in Cu SAC/P-1 compared to that of Cu SAC at the same position (Fig. S27), leading to the orbital and electronic interactions between Cu and P more apparent in Cu SAC/P-1 [27]. Thus, the d-band center (ϵ_d , relative to the Fermi energy level, Fig. 5c) of Cu SAC/P-1 (−3.33 eV) had a positive shift and more antibonding states of adsorbed intermediates above the Fermi energy level compared to Cu SAC (−3.41 eV), which implied that Cu SAC/P-1 had strong binding energy with intermediates and favors the formation of OOH* intermediate [57,58]. To test this speculation, the adsorption energy of O₂ and the electron density difference of OOH* intermediate in different structures were calculated. Fig. S28

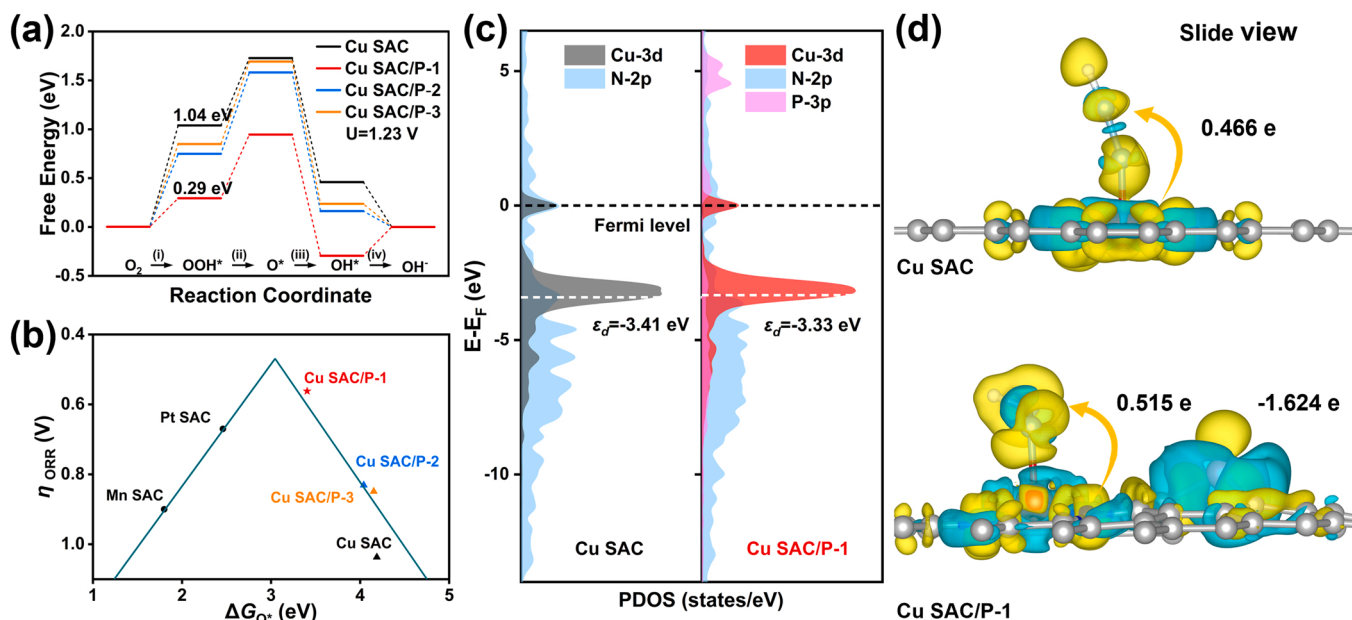


Fig. 5. The density functional theory (DFT) calculations results for ORR. (a) Gibbs free energy profiles of various models at 0 V overpotential. (b) The volcano plot of overpotential (η_{ORR}) for O* adsorption free energy (ΔG_{O^*}) of different structures. (c) The calculated PDOS of the Cu SAC and Cu SAC/P-1. (d) Bader charge and electron density difference plot of the OOH* intermediate adsorbed on Cu SAC and Cu SAC/P-1. Yellow and cyan stand for charge accumulation and depletion, respectively. The isosurface value is 0.0025 $e/\text{\AA}^3$.

showed the stronger adsorption of O₂ on the Cu atom of Cu SAC/P, which was consistent with the result of the previous TPD experiment. As the first step of ORR, Cu SAC/P-1 with the strongest O₂ adsorption energy (−0.334 eV) will facilitate the formation of ORR intermediates, enabling the ORR process to proceed smoothly [59]. Additionally, the electron density difference plot and bader charge analysis of OOH* intermediate adsorption on Cu SAC and Cu SAC/P-1 were shown in Fig. 5d and S29, revealing that the higher amount of charge transferred from Cu to OOH* intermediate for Cu SAC/P-1. It was also indicated that the OOH* intermediate binded more strongly on Cu SAC/P-1, which helped the Cu atom to trap the OOH* intermediate and reduced the energy barrier of the RDS [60]. The above results indicated that the Cu SAC/P catalysts possess excellent ORR electrochemical catalytic activity.

4. Conclusions

In summary, the Cu SAC/P catalysts have been prepared by the self-assembly of effective precursor and the strategy of secondary heteroatomic phosphorus doping. Since the doping of heteroatomic phosphorus enhanced the adsorption of the oxygen reduction reaction (ORR) intermediates at the copper atom in alkaline media, the Cu SAC/P-700 sample exhibits superior ORR activity and outstanding cycle stability performance for the zinc-air battery. Density functional theory calculations demonstrate that the doping of secondary heteroatomic phosphorus effectively optimizes the density of states distribution and *d*-band center of the Cu atom, thus improving the adsorption of the intermediate and decreasing the reaction energy barrier to boost ORR activity. This work delves into the electronic structure relationship between copper atom and heteroatomic phosphorus at the atomic level, which provides relevant insights for the development of high efficiency electrochemical catalysts with secondary heteroatom doping.

CRediT authorship contribution statement

Lei Wang: Conceptualization, Methodology, Investigation, Formal analysis, Writing – original draft. **Wen-Wen Tian:** Writing – review & editing. **Wenlin Zhang:** Supervision, Writing – review & editing. **Fengshou Yu:** Writing-review & editing. **Zhong-Yong Yuan:** Supervision, Writing-review & editing.

Declaration of Competing Interest

The authors declare that they have no known competing financial interests or personal relationships that could have appeared to influence the work reported in this paper.

Acknowledgments

This work was supported by the National Natural Science Foundation of China (No. 21905073 and 22179065), Hundred Talents Project of Hebei Province (No. E2019050015), Natural Science Foundation of Hebei Province (No. B2021202010), and Fundamental Research Foundation of Hebei University of Technology (JBKYTD2001).

Appendix A. Supporting information

Supplementary data associated with this article can be found in the online version at [doi:10.1016/j.apcatb.2023.123043](https://doi.org/10.1016/j.apcatb.2023.123043).

References

- [1] G. Fu, J. Wang, Y. Chen, Y. Liu, Y. Tang, J.B. Goodenough, J.-M. Lee, Exploring indium-based ternary thiospinel as conceivable high-potential air-cathode for rechargeable zn-air batteries, *Adv. Energy Mater.* 8 (2018) 1802263.
- [2] H. Jiang, Y. Liu, W. Li, J. Li, Co nanoparticles confined in 3D nitrogen-doped porous carbon foams as bifunctional electrocatalysts for long-life rechargeable Zn-Air batteries, *Small* 14 (2018) 1703739.
- [3] J.-N. Liu, C.-X. Zhao, J. Wang, D. Ren, B.-Q. Li, Q. Zhang, A brief history of zinc-air batteries: 140 years of epic adventures, *Energy Environ. Sci.* 15 (2022) 4542–4553.
- [4] M. Qian, M. Xu, S. Zhou, J. Tian, T. Taylor Isimjan, Z. Shi, X. Yang, Template synthesis of two-dimensional ternary nickel-cobalt-nitrogen co-doped porous carbon film: Promoting the conductivity and more active sites for oxygen reduction, *J. Colloid Interface Sci.* 564 (2020) 276–285.
- [5] H. Chen, S. Chen, Z. Zhang, L. Sheng, J. Zhao, W. Fu, S. Xi, R. Si, L. Wang, M. Fan, B. Yang, Single-atom-induced adsorption optimization of adjacent sites boosted oxygen evolution reaction, *ACS Catal.* 12 (2022) 13482–13491.
- [6] C. Tang, H.-S. Wang, H.-F. Wang, Q. Zhang, G.-L. Tian, J.-Q. Nie, F. Wei, Spatially confined hybridization of nanometer-sized NiFe hydroxides into nitrogen-doped graphene frameworks leading to superior oxygen evolution reactivity, *Adv. Mater.* 27 (2015) 4516–4522.
- [7] X. Han, X. Wu, C. Zhong, Y. Deng, N. Zhao, W. Hu, NiCo₂S₄ nanocrystals anchored on nitrogen-doped carbon nanotubes as a highly efficient bifunctional electrocatalyst for rechargeable zinc-air batteries, *Nano Energy* 31 (2017) 541–550.
- [8] C. Hu, Q. Liang, Y. Yang, Q. Peng, Z. Luo, J. Dong, T.T. Isimjan, X. Yang, Conductivity-enhanced porous N/P co-doped metal-free carbon significantly enhances oxygen reduction kinetics for aqueous/flexible zinc-air batteries, *J. Colloid Interface Sci.* 633 (2023) 500–510.
- [9] K. Zeng, X. Zheng, C. Li, J. Yan, J.H. Tian, C. Jin, P. Strasser, R. Yang, Recent advances in non-noble bifunctional oxygen electrocatalysts toward large-scale production, *Adv. Funct. Mater.* 30 (2020) 2000503.
- [10] L. Dai, Y. Xue, L. Qu, H.-J. Choi, J.-B. Baek, Metal-free catalysts for oxygen reduction reaction, *Chem. Rev.* 115 (2015) 4823–4892.
- [11] J. Yin, Y. Li, F. Lv, Q. Fan, Y.-Q. Zhao, Q. Zhang, W. Wang, F. Cheng, P. Xi, S. Guo, NiO/CoN porous nanowires as efficient bifunctional catalysts for Zn-air batteries, *ACS Nano* 11 (2017) 2275–2283.
- [12] H.F. Wang, C. Tang, B. Wang, B.Q. Li, Q. Zhang, Bifunctional transition metal hydroxysulfides: room-temperature sulfuration and their applications in Zn-Air batteries, *Adv. Mater.* 29 (2017) 1702327.
- [13] Y. Zhang, L. Qian, W. Zhao, X. Li, X. Huang, X. Mai, Z. Wang, Q. Shao, X. Yan, Z. Guo, Highly efficient Fe-N-C nanoparticles modified porous graphene composites for oxygen reduction reaction, *J. Electrochem. Soc.* 165 (2018) H510–H516.
- [14] B.S. Natinsky, C. Liu, Two are better than one, *Nat. Chem.* 11 (2019) 200–201.
- [15] P. Peng, L. Shi, F. Huo, C. Mi, X. Wu, S. Zhang, Z. Xiang, A pyrolysis-free path toward superiorly catalytic nitrogen-coordinated single atom, *Sci. Adv.* 5 (2019) eaaw2322.
- [16] Y. Qu, Z. Li, W. Chen, Y. Lin, T. Yuan, Z. Yang, C. Zhao, J. Wang, C. Zhao, X. Wang, F. Zhou, Z. Zhuang, Y. Wu, Y. Li, Direct transformation of bulk copper into copper single sites via emitting and trapping of atoms, *Nat. Catal.* 1 (2018) 781–786.
- [17] H. Wu, H. Li, X. Zhao, Q. Liu, J. Wang, J. Xiao, S. Xie, R. Si, F. Yang, S. Miao, X. Guo, G. Wang, X. Bao, Highly doped and exposed Cu-N active sites within graphene towards efficient oxygen reduction for zinc-air batteries, *Energy Environ. Sci.* 9 (2016) 3736–3745.
- [18] G. Han, Y. Zheng, X. Zhang, Z. Wang, Y. Gong, C. Du, M.N. Banis, Y.-M. Yiu, T.-K. Sham, L. Gu, Y. Sun, Y. Wang, J. Wang, Y. Gao, G. Yin, X. Sun, High loading single-atom Cu dispersed on graphene for efficient oxygen reduction reaction, *Nano Energy* 66 (2019), 104088.
- [19] N.K. Wagh, S.S. Shinde, C.H. Lee, J.-Y. Jung, D.-H. Kim, S.-H. Kim, C. Lin, S.U. Lee, J.-H. Lee, Densely colonized isolated Cu-N single sites for efficient bifunctional electrocatalysts and rechargeable advanced Zn-air batteries, *Appl. Catal. B-Environ.* 268 (2020), 118746.
- [20] Y. Chen, S. Ji, S. Zhao, W. Chen, J. Dong, W.-C. Cheong, R. Shen, X. Wen, L. Zheng, A.I. Rykov, S. Cai, H. Tang, Z. Zhuang, C. Chen, Q. Peng, D. Wang, Y. Li, Enhanced oxygen reduction with single-atomic-site iron catalysts for a zinc-air battery and hydrogen-air fuel cell, *Nat. Commun.* 9 (2018) 5422.
- [21] Z. Jiang, W. Sun, H. Shang, W. Chen, T. Sun, H. Li, J. Dong, J. Zhou, Z. Li, Y. Wang, R. Cao, R. Sarangi, Z. Yang, D. Wang, J. Zhang, Y. Li, Atomic interface effect of a single atom copper catalyst for enhanced oxygen reduction reactions, *Energy Environ. Sci.* 12 (2019) 3508–3514.
- [22] X. Zhou, M.-K. Ke, G.-X. Huang, C. Chen, W. Chen, K. Liang, Y. Qu, J. Yang, Y. Wang, F. Li, H.-Q. Yu, Y. Wu, Identification of Fenton-like active Cu sites by heteroatom modulation of electronic density, *Proc. Natl. Acad. Sci.* 119 (2022), e2119492119.
- [23] G. Yang, J. Zhu, P. Yuan, Y. Hu, G. Qu, B.-A. Lu, X. Xue, H. Yin, W. Cheng, J. Cheng, W. Xu, J. Li, J. Hu, S. Mu, J.-N. Zhang, Regulating Fe-spin state by atomically dispersed Mn-N in Fe-N-C catalysts with high oxygen reduction activity, *Nat. Commun.* 12 (2021) 1734.
- [24] T. Najam, S.S.A. Shah, W. Ding, J. Jiang, L. Jia, W. Yao, L. Li, Z. Wei, An efficient anti-poisoning catalyst against SO_x, NO_x, and PO_x: P, N-doped carbon for oxygen reduction in acidic media, *Angew. Chem. Int. Ed.* 57 (2018) 15101–15106.
- [25] J. Quilez-Bermejo, E. Morallon, D. Cazorla-Amoros, Metal-free heteroatom-doped carbon-based catalysts for ORR: a critical assessment about the role of heteroatoms, *Carbon* 165 (2020) 434–454.
- [26] H. Yin, P. Yuan, B.-A. Lu, H. Xia, K. Guo, G. Yang, G. Qu, D. Xue, Y. Hu, J. Cheng, S. Mu, J.-N. Zhang, Phosphorus-driven electron delocalization on edge-type FeN₄ active sites for oxygen reduction in acid medium, *ACS Catal.* 11 (2021) 12754–12762.
- [27] X. Sun, L. Sun, G. Li, Y. Tuo, C. Ye, J. Yang, J. Low, X. Yu, J.H. Bitter, Y. Lei, D. Wang, Y. Li, Phosphorus tailors the D-band center of copper atomic sites for

- efficient CO₂ photoreduction under visible-light irradiation, *Angew. Chem. Int. Ed.* 61 (2022), e202207677.
- [28] D.-W. Wang, D. Su, Heterogeneous nanocarbon materials for oxygen reduction reaction, *Energy Environ. Sci.* 7 (2014) 576–591.
- [29] C.-X. Zhao, J.-N. Liu, J. Wang, C. Wang, X. Guo, X.-Y. Li, X. Chen, L. Song, B.-Q. Li, Q. Zhang, A clicking confinement strategy to fabricate transition metal single-atom sites for bifunctional oxygen electrocatalysis, *Sci. Adv.* 8 (2022) eabn5091.
- [30] X. Feng, Y. Bai, M. Liu, Y. Li, H. Yang, X. Wang, C. Wu, Untangling the respective effects of heteroatom-doped carbon materials in batteries, supercapacitors and the ORR to design high performance materials, *Energy Environ. Sci.* 14 (2021) 2036–2089.
- [31] D. Guo, R. Shibuya, C. Akiba, S. Saji, T. Kondo, J. Nakamura, Active sites of nitrogen-doped carbon materials for oxygen reduction reaction clarified using model catalysts, *Science* 351 (2016) 361–365.
- [32] W.-W. Tian, J.-T. Ren, Z.-Y. Yuan, In-situ cobalt-nickel alloy catalyzed nitrogen-doped carbon nanotube arrays as superior freestanding air electrodes for flexible zinc-air and aluminum-air batteries, *Appl. Catal. B-Environ.* 317 (2022), 121764.
- [33] R. Wang, X.-Y. Dong, J. Du, J.-Y. Zhao, S.-Q. Zang, MOF-derived bifunctional Cu₃P nanoparticles coated by a N,P-codoped carbon shell for hydrogen evolution and oxygen reduction, *Adv. Mater.* 30 (2017) 1703711.
- [34] J. Guo, W. Zhang, L.-H. Zhang, D. Chen, J. Zhan, X. Wang, N.R. Shiju, F. Yu, Control over electrochemical CO₂ reduction selectivity by coordination engineering of tin single-atom catalysts, *Adv. Sci.* 8 (2021) 2102884.
- [35] D. Chen, L.H. Zhang, J. Du, H. Wang, J. Guo, J. Zhan, F. Li, F. Yu, A Tandem, Strategy for enhancing electrochemical CO₂ reduction activity of single-atom Cu-S₁N₃ catalysts via integration with Cu nanoclusters, *Angew. Chem. Int. Ed.* 60 (2021) 24022–24027.
- [36] Y. Cheng, S. He, S. Lu, J.P. Veder, B. Johannessen, L. Thomsen, M. Saunders, T. Becker, R. De Marco, Q. Li, Sz Yang, S.P. Jiang, Iron single atoms on graphene as nonprecious metal catalysts for high-temperature polymer electrolyte membrane fuel cells, *Adv. Sci.* 6 (2019) 1802066.
- [37] S. Li, S. Zhao, X. Lu, M. Ceccato, X.-M. Hu, A. Roldan, J. Catalano, M. Liu, T. Skrydstrup, K. Daasbjerg, Low-Valence Zn^{δ+} (0<δ<2) single-atom material as highly efficient electrocatalyst for CO₂ Reduction, *Angew. Chem. Int. Ed.* 60 (2021) 22826–22832.
- [38] J.-T. Ren, Y.-D. Ying, Y.-P. Liu, W. Li, Z.-Y. Yuan, Charge redistribution caused by sulfur doping of bimetal FeCo phosphides supported on heteroatoms-doped graphene for Zn-air batteries with stable cycling, *J. Energy Chem.* 71 (2022) 619–630.
- [39] M. Guo, Z. Huang, Y. Qu, L. Wang, H. Li, T.T. Isimjan, X. Yang, Synergistic effect and nanostructure engineering of three-dimensionally hollow mesoporous spherical Cu₃P/TiO₂ in aqueous/flexible Zn-air batteries, *Appl. Catal. B-Environ.* 320 (2023), 121991.
- [40] M. Guo, M. Xu, Y. Qu, C. Hu, P. Yan, T.T. Isimjan, X. Yang, Electronic/mass transport increased hollow porous Cu₃P/MoP nanospheres with strong electronic interaction for promoting oxygen reduction in Zn-air batteries, *Appl. Catal. B-Environ.* 297 (2021), 120415.
- [41] L. Zong, K. Fan, W. Wu, L. Cui, L. Zhang, B. Johannessen, D. Qi, H. Yin, Y. Wang, P. Liu, L. Wang, H. Zhao, Anchoring single copper atoms to microporous carbon spheres as high-performance electrocatalyst for oxygen reduction reaction, *Adv. Funct. Mater.* 31 (2021) 2104864.
- [42] J. Yang, W. Liu, M. Xu, X. Liu, H. Qi, L. Zhang, X. Yang, S. Niu, D. Zhou, Y. Liu, Y. Su, J.-F. Li, Z.-Q. Tian, W. Zhou, A. Wang, T. Zhang, Dynamic behavior of single-atom catalysts in electrocatalysis: identification of Cu-N₃ as an active site for the oxygen reduction reaction, *J. Am. Chem. Soc.* 143 (2021) 14530–14539.
- [43] H. Zhao, R. Yu, S. Ma, K. Xu, Y. Chen, K. Jiang, Y. Fang, C. Zhu, X. Liu, Y. Tang, L. Wu, Y. Wu, Q. Jiang, P. He, Z. Liu, L. Tan, The role of Cu₁-O₂ species in single-atom Cu/ZrO₂ catalyst for CO₂ hydrogenation, *Nat. Catal.* (2022) 818–831.
- [44] T. Sun, Y. Li, T. Cui, L. Xu, Y.-G. Wang, W. Chen, P. Zhang, T. Zheng, X. Fu, S. Zhang, Z. Zhang, D. Wang, Y. Li, Engineering of coordination environment and multiscale structure in single-site copper catalyst for superior electrocatalytic oxygen reduction, *Nano Lett.* 20 (2020) 6206–6214.
- [45] F. Li, G.F. Han, H.J. Noh, S.J. Kim, Y.L. Lu, H.Y. Jeong, Z.P. Fu, J.B. Baek, Boosting oxygen reduction catalysis with abundant copper single atom active sites, *Energy Environ. Sci.* 11 (2018) 2263–2269.
- [46] W. Zhang, L. Wang, L.-H. Zhang, D. Chen, Y. Zhang, D. Yang, N. Yan, F. Yu, Creating hybrid coordination environment in Fe-based single atom catalyst for efficient oxygen reduction, *ChemSusChem* 15 (2022), e202200195.
- [47] T. Wang, X. Cao, H. Qin, L. Shang, S. Zheng, F. Fang, L. Jiao, P. -Block atomically dispersed antimony catalyst for highly efficient oxygen reduction reaction, *Angew. Chem. Int. Ed.* 60 (2021) 21237–21241.
- [48] Z. Li, Z. Zhuang, F. Lv, H. Zhu, L. Zhou, M. Luo, J. Zhu, Z. Lang, S. Feng, W. Chen, L. Mai, S. Guo, The marriage of the FeN₄ moiety and MXene boosts oxygen reduction catalysis: Fe 3d electron delocalization matters, *Adv. Mater.* 30 (2018) 1803220.
- [49] J. Ryu, H. Jang, J. Park, Y. Yoo, M. Park, J. Cho, Seed-mediated atomic-scale reconstruction of silver manganate nanoplates for oxygen reduction towards high-energy aluminum-air flow batteries, *Nat. Commun.* 9 (2018) 3715.
- [50] P. Chen, T. Zhou, L. Xing, K. Xu, Y. Tong, H. Xie, L. Zhang, W. Yan, W. Chu, C. Wu, Y. Xie, Atomically dispersed iron-nitrogen species as electrocatalysts for bifunctional oxygen evolution and reduction reactions, *Angew. Chem. Int. Ed.* 56 (2016) 610–614.
- [51] M. Che, Nobel Prize in chemistry 1912 to Sabatier: organic chemistry or catalysis? *Catal. Today* 218 (2013) 162–171.
- [52] J.K. Nørskov, J. Rossmeisl, A. Logadottir, L. Lindqvist, J.R. Kitchin, T. Bligaard, H. Jónsson, Origin of the overpotential for oxygen reduction at a fuel-cell cathode, *J. Phys. Chem. B* 108 (2004) 17886–17892.
- [53] H. Shang, X. Zhou, J. Dong, A. Li, X. Zhao, Q. Liu, Y. Lin, J. Pei, Z. Li, Z. Jiang, D. Zhou, L. Zheng, Y. Wang, J. Zhou, Z. Yang, R. Cao, R. Sarangi, T. Sun, X. Yang, X. Zheng, W. Yan, Z. Zhuang, J. Li, W. Chen, D. Wang, J. Zhang, Y. Li, Engineering unsymmetrically coordinated Cu-S₁N₃ single atom sites with enhanced oxygen reduction activity, *Nat. Commun.* 11 (2020) 3049.
- [54] B. Liu, R. Feng, M. Busch, S. Wang, H. Wu, P. Liu, J. Gu, A. Bahadoran, D. Matsumura, T. Tsuji, D. Zhang, F. Song, Q. Liu, Synergistic hybrid electrocatalysts of platinum alloy and single-atom platinum for an efficient and durable oxygen reduction reaction, *ACS Nano* 16 (2022) 14121–14133.
- [55] Z. Pei, X.F. Lu, H. Zhang, Y. Li, D. Luan, X.W. Lou, Highly efficient electrocatalytic oxygen evolution over atomically dispersed synergistic Ni/Co dual sites, *Angew. Chem. Int. Ed.* 61 (2022), e202207537.
- [56] J. Zhang, Y. Zhao, C. Chen, Y.-C. Huang, C.-L. Dong, C.-J. Chen, R.-S. Liu, C. Wang, K. Yan, Y. Li, G. Wang, Tuning the coordination environment in single-atom catalysts to achieve highly efficient oxygen reduction reactions, *J. Am. Chem. Soc.* 141 (2019) 20118–20126.
- [57] J.K. Nørskov, F. Abild-Pedersen, F. Studt, T. Bligaard, Density functional theory in surface chemistry and catalysis, *Proc. Natl. Acad. Sci.* 108 (2011) 937–943.
- [58] F. Yu, J. Zhan, D. Chen, J. Guo, S. Zhang, L.-H. Zhang, Electronic states regulation induced by the synergistic effect of Cu clusters and Cu-S₁N₃ sites boosting electrocatalytic performance, *Adv. Funct. Mater.* (2023) 2214425.
- [59] S. Wang, E. Zhu, Y. Huang, H. Heinz, Direct correlation of oxygen adsorption on platinum-electrolyte interfaces with the activity in the oxygen reduction reaction, *Sci. Adv.* 7 (2021) eabb1435.
- [60] Z. Li, S. Ji, C. Xu, L. Leng, H. Liu, J.H. Horton, L. Du, J. Gao, C. He, X. Qi, Q. Xu, J. Zhu, Engineering the electronic structure of single-atom iron sites with boosted oxygen bifunctional activity for zinc-air batteries, *Adv. Mater.* 35 (2023) 2209644.